Supplementary Information:
Experimental realization of on-chip few-photon control around exceptional points

Pengtao Song[1,2]*, Xinhui Ruan[3,1,2]*, Haijin Ding[3], Shengyong Li[3], Ming Chen[1], Ran Huang[1], Le-Man Kuang[1], Qianchuan Zhao[3], Jaw-Shen Tsai[4,5], Hui Jing[1], Lan Yang[6], Franco Nori[4,7,8], Dongning Zheng[2,9]†, Yu-xi Liu[10], Jing Zhang[11,12]†, Zhihui Peng[1]†

Affiliations:

[1]Key Laboratory of Low-Dimensional Quantum Structures and Quantum Control of Ministry of Education, Department of Physics and Synergetic Innovation Center of Quantum Effects and Applications, Hunan Normal University, Changsha 410081, China

[2]Institute of Physics, Chinese Academy of Sciences, Beijing 100190, China

[3]Department of Automation, Tsinghua University, Beijing 100084, China

[4]Center for Quantum Computing, RIKEN, Saitama 351–0198, Japan

[5]Graduate School of Science, Tokyo University of Science, 1–3 Kagurazaka, Shinjuku, Tokyo 162–0825, Japan

[6]Department of Electrical and Systems Engineering, Washington University, St. Louis, MO 63130, USA

[7]Theoretical Quantum Physics Laboratory, Cluster for Pioneering Research, RIKEN, Saitama 351-0198, Japan

[8]University of Michigan, Ann Arbor, Michigan 48109-1040, USA

[9]School of Physical Sciences, University of Chinese Academy of Sciences, Beijing 100190, China

[10]School of Integrated Circuits,Tsinghua University, Beijing 100084, China

[11]School of Automation Science and Engineering, Xi'an Jiaotong University, Xi'an 710049, China

[12]MOE Key Lab for Intelligent Networks and Network Security, Xi'an Jiaotong University, Xi'an 710049, China

*These authors contributed equally to this work

†e-mail: dzheng@iphy.ac.cn, zhangjing2022@xjtu.edu.cn,
zhihui.peng@hunnu.edu.cn

I. DETAILS OF THE EXPERIMENTAL SETUPS AND THE MEASUREMENT CALIBRATIONS

A. Parameters of the experimental system

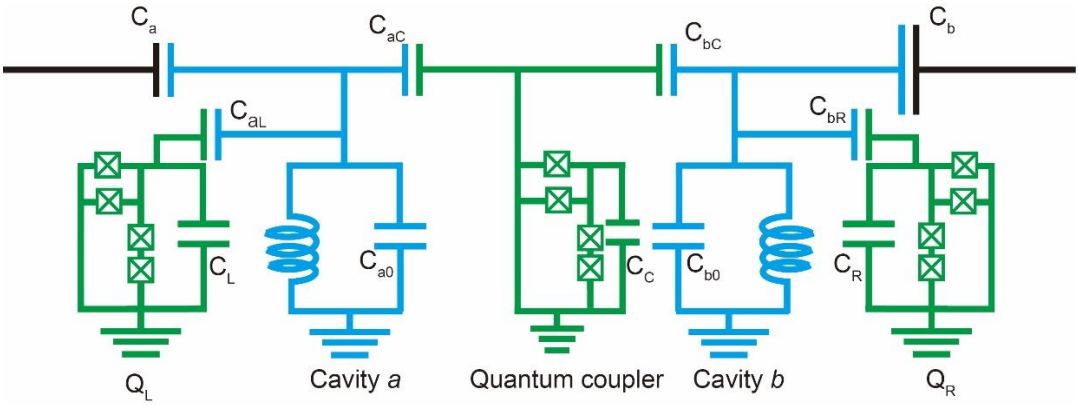

Figure S1. Circuit diagram of the superconducting quantum chip. The quantum coupler (a tuneable-gap flux qubit) is coupled to cavity *a* and cavity *b* through capacitors C_{aC} and C_{bC}, respectively. The eigen-frequencies of the two cavities can be tuned by capacitive coupling to two gap-tuneable flux qubits Q_L and qubit Q_R through capacitors C_{aL} and C_{bR}, respectively. The two cavities are coupled to the environment through capacitors C_a and C_b, respectively.

The superconducting quantum chip consists of two CPW cavities and three tuneable-gap flux qubits [S1] , as shown in Fig. S1. The two cavities are designed with the same eigen-frequency but different decay rates which are mainly controlled by the coupling capacitor between cavities and transmission line (C_a and C_b, respectively). The direct coupling between the two cavities is negligible and we can control the coupling strength between the two cavities by a quantum coupler. The flux qubit works as a quantum coupler which has been demonstrated elsewhere in superconducting quantum information processing [S2] , [S3] . In our experiments, the flux qubits are with large anharmonicity and thus work as good two-level systems. The additional two flux qubits, i.e., Q_L and Q_R in Fig. S1, are used for tuning the resonant frequencies of the two

cavities slightly and inducing nonlinearity in the two cavities. Each flux qubit has two independent control-lines to inject external magnetic fields. One line is for controlling the flux in α loop, and the other line is for controlling the flux in the main loop. We do some simulations before fabricating the chip, and have $C_{aL} \approx C_{bR} \approx 4.8\,fF$, $C_L \approx C_R \approx 105.8\,fF$, $C_{aC} \approx C_{bC} \approx 3.1\,fF$, $C_a \approx 17\,fF$, $C_b \approx 30\,fF$. These circuit parameters agree well with the extracted parameters in experiments. The parameters of the experimental system are show in Table. S1.

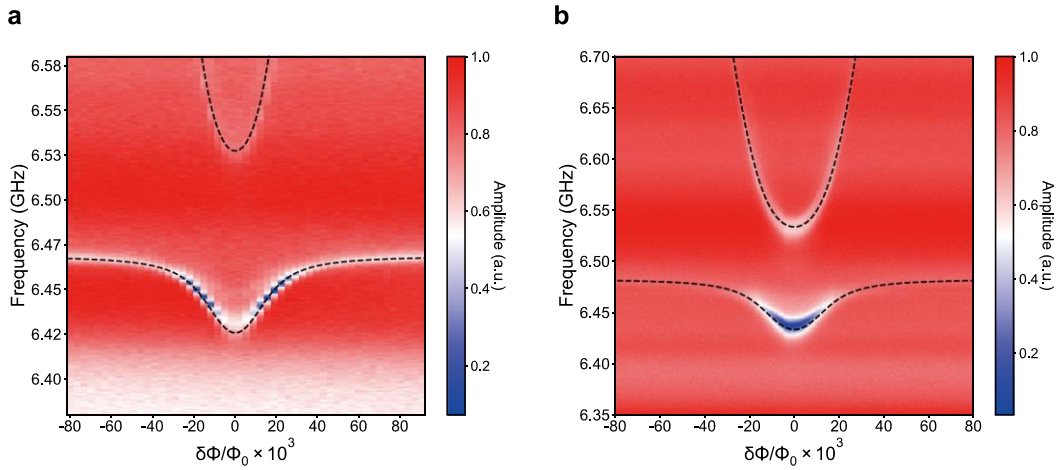

Figure S2. Observation of vacuum Rabi splitting through normalized amplitudes of reflection coefficients versus the flux bias δΦ. a, The vacuum Rabi splitting between cavity a and Q_L. **b,** The vacuum Rabi splitting between cavity b and Q_R. The dashed lines are the theoretical fitting curves.

Table S1. Parameters of the experimental system. f_{c0} is the bare frequency of the cavity without qubit, and f_{c1} is the frequency of the cavity when the cavities are tuned by the left and right qubits. $\kappa_{a,b}$ are the decay rates of the two cavities. $\gamma_\perp$ is the decoherence rate of the qubit at the optimal point extracted from the two-tone spectroscopy. I_p is the persistent current of the flux qubit. $\tilde{g}$ is the coupling strength between the cavity and the qubit.

Modes	f_{c0} **(GHz)**	f_{c1} **(GHz)**	$\frac{\kappa_{a,b}(\gamma_\perp)}{2\pi}$ **(MHz)**	I_p **(GHz/mΦ₀)**	$\frac{\tilde{g}}{2\pi}$ **(MHz)**
Q_L	-	-	7.3	0.03	50
Q_R	-	-	4.8	0.03	50
Q_C	-	-	10.0	0.38	71
Cavity a	6.469	6.474	7.7	-	-
Cavity b	6.483	6.474	20.9	-	-

B. Calibration of the photon numbers inside the cavities

We calibrate the measurement system with the ac-Stark shift [S4] , [S5] . Consider a system that a cavity is coupled to a qubit in a dispersive regime. The transition frequency of the qubit will be shifted by the photon number stored in the cavity which is called ac-Stark shift. The frequency shift of qubit is $\delta\omega_q = \left(2\langle n\rangle \tilde{g}^2\right)/\Delta$, where $\langle n\rangle$ is the average photon number stored in the cavity. $\tilde{g}$ and Δ are the coupling strength and frequency detuning between the qubit and the cavity.

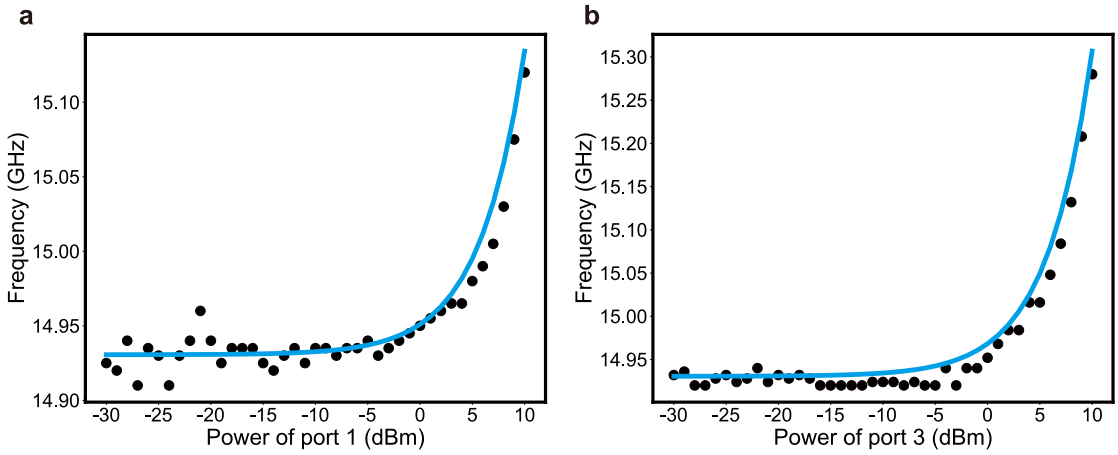

Figure S3. AC-Stark shift of the quantum coupler. The two-tone spectra of Q_c when the cavity a is driven (**a**) or the cavity b is driven (**b**). The black dots are the experimental data points while the blue solid lines are the fitting curves using Eq. (S.1).

We use the flux qubit Q_c, which is biased at the optimal point with transition frequency 14.93 GHz, to calibrate the measurement system for few-photon nonreciprocity transmission experiment. Here, the effective coupling between two cavities is negligible and the EP system is at the broken-symmetric regime. We obtain the ac-Stark shift by performing standard two-tone spectroscopy and changing $\langle n\rangle$ with different probing power from VNA. We set the probing power from VNA as P_{VNA} (the unit is dBm). The total attenuation from VNA port to chip is as α_{tot} (unit is dB). The resonant frequency of cavity is ω_c. The decay rate of cavity is $\kappa_{a(b)}$. Then, the frequency shift of qubit can be calculated by

$$\delta\omega_q = \frac{2\tilde{g}^2}{\Delta}\frac{10^{\left(\frac{P_{\mathrm{VNA}}-\alpha_{\mathrm{tot}}}{10}-3\right)}}{\hbar\omega_c\kappa_{a(b)}}, \tag{S.1}$$

with $\hbar$ as the reduced Plank constant.

We then drive cavity a (cavity b) through the port 1 (port 3) of VNA, and measure the transition frequency of Q_c versus the probing power as shown in Fig. S3. By fitting the theoretical curves using Eq. (S.1), we can obtain the attenuations of two different input lines, which are 114.5 dB and 107.5 dB, respectively. Here, the ac-Stark shift of the qubit per photon in cavity is 2.0 MHz. Then, we adjust the attenuators mounted at the two input lines at room temperature to make sure that the attenuations of the two input lines are with the same value of 107.5 dB. In this way, the probing power on chip keeps constant in few-photon nonreciprocity experiments. Once we get the total attenuation $\alpha_{\text{tot}} = 107.5$ dB, we can estimate the photon number in few-photon nonreciprocity experiments using

$$\langle n \rangle = \frac{10^{\left(\frac{P_{\text{VNA}} - \alpha_{\text{tot}}}{10} - 3\right)}}{\hbar \omega_c \kappa_a}. \tag{S.2}$$

The photon number we mentioned in this paper is calculated for the cavity with higher quality-factor (cavity a). The noise spectral density of the preamplifier (Model: LNF-LNC0.3_14A with a nominal noise temperature around 3.6 K) placed at temperature of 3.2 K is $2\pi S(\omega) = k_B T_n = 1.05 \times 10^{-22}$ W/Hz, which corresponds to the effective noise temperature $T_n = 7.5$ K of the amplifier at the input port. Therefore, we can conclude that the calibration precision is better than ± 3dB.

II. BIFURCATION IN THE VICINITY OF THE EXCEPTIONAL POINT

A. Hamiltonian of the coupled system

As shown in Fig. S4, the flux qubit that we consider here is a superconducting loop with four Josephson junctions, by which the minimum energy gap of the qubit can be adjusted through a dc-SQUID (α loop) [S2] . Traditionally, a flux qubit consists of three Josephson junctions, i.e., two larger junctions with the same Josephson energy E_J and capacitance C_J and a smaller junction with Josephson energy αE_J and capacitance αC_J ($0.5 < \alpha < 1$). The existence of the α loop, i.e., the smaller junction is replaced

by a dc-SQUID, allows that the α value can be tuned by the external flux Φ_α piercing the loop of the dc-SQUID. When the biased flux Φ is close to $\Phi = \Phi_0 / 2$, the Hamiltonian of the flux qubit can be written as

$$H_q = -\varepsilon(\Phi)\sigma_z / 2 - \Delta(\Phi_\alpha)\sigma_x / 2, \quad \text{(S.3)}$$

where Φ_0 is the flux quantum, $\sigma_{z,x}$ are the Pauli spin matrices, Δ is the minimum

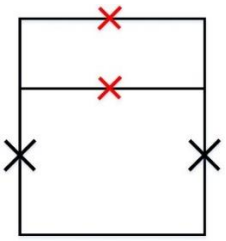

Figure S4. Simplified circuit diagram of the gap-tuneable flux qubit. The main loop is formed by two larger junctions (black) and a dc-SQUID. The α loop of the dc-SQUID is formed by two smaller junctions (red).

energy gap, $\varepsilon \approx 2I_p(\Phi - \Phi_0 / 2) = 2I_p\delta\Phi$, and $I_p \approx 2\pi\alpha E_J / \Phi_0$ is the persistent current in the main loop of the flux qubit. The flux qubit behaves as a two-level system, and we can use the following Jaynes-Cummings-type Hamiltonian to describe the flux qubit capacitively coupled to a cavity mode a as [S2],

$$H_{JC} = \frac{1}{2}\omega_q\sigma_z + \omega_c a^\dagger a + g_{qc}(a^\dagger\sigma_- + a\sigma_+). \quad \text{(S.4)}$$

Here, $\omega_q = \sqrt{\varepsilon^2(\Phi) + \Delta^2(\Phi_\alpha)}$ is the transition frequency between the two lowest energy states of the flux qubit, ω_c is the resonance frequency of the cavity mode, and g_{qc} is the coupling strength between the qubit and the cavity mode. We can use H_{JC} to describe the system composed of the left (right) qubit and the cavity mode in the left (right) superconducting resonator.

For a system with two cavity modes a and b which are indirectly coupled with each other and mediated by a flux qubit (quantum coupler), the Hamiltonian can be expressed as

$$H_c = \omega_a a^\dagger a + \omega_b b^\dagger b + \omega_q\sigma_+\sigma_- + g_a\left(a^\dagger\sigma_- + a\sigma_+\right) + g_b\left(b^\dagger\sigma_- + b\sigma_+\right). \quad \text{(S.5)}$$

Here, $a(b)$ is the annihilation operator of the high-Q (low-Q) cavity mode. σ_- and σ_+ are the ladder operators of qubit. $g_a(g_b)$ is the coupling strength between the cavity mode $a(b)$ and the mediated flux qubit. $\omega_i\,(i=a,b,q)$ are the resonance frequencies of the two cavities and the qubit. In our experiments, the coupling strengths g_a and g_b are designed to be close to each other, i.e., $g_a \approx g_b$.

B. Exceptional point of the coupled-resonator system

In order to understand the mechanism of the system, we firstly consider the Hamiltonian in Eq. (S.5). In the rotating frame at the driving frequency ω_d, we introduce the unitary transformation $U=\exp(-i\omega_d\sigma_z - i\omega_d a^\dagger a - i\omega_d b^\dagger b)$ and the Hamiltonian in Eq. (S.5) can be rewritten as

$$H_1 = \Delta_a a^\dagger a + \Delta_b b^\dagger b + \Delta_q \sigma_+\sigma_- + g_a\left(a^\dagger\sigma_- + a\sigma_+\right) + g_b\left(b^\dagger\sigma_- + b\sigma_+\right), \tag{S.6}$$

where $\Delta_i = \omega_i - \omega_d\,(i=a,b,q)$ is the effective frequency of the cavity mode or the qubit. The dynamical equation of the system can be written as [S6] ,[S7]

$$\frac{d}{dt}\left\langle\hat{Q}\right\rangle = -i\left\langle\left[\hat{Q},H_1\right]\right\rangle + \hat{\mathcal{L}}\hat{Q}, \tag{S.7}$$

where $\hat{Q}$ is the operator of the system and $\langle\cdot\rangle$ denotes the average value of an operator. The Liouville superoperator $\hat{\mathcal{L}}\hat{Q}$, representing the dissipation terms of the cavity modes and the qubit, is defined as

$$\begin{aligned}\hat{\mathcal{L}}\hat{Q} = {}& \frac{\kappa_a}{2}\left(2a^\dagger\hat{Q}a - \hat{Q}a^\dagger a - a^\dagger a\hat{Q}\right) + \frac{\kappa_b}{2}\left(2b^\dagger\hat{Q}b - \hat{Q}b^\dagger b - b^\dagger b\hat{Q}\right)\\ & + \frac{\gamma_{\parallel}}{2}\left(2\sigma_+\hat{Q}\sigma_- - \hat{Q}\sigma_+\sigma_- - \sigma_+\sigma_-\hat{Q}\right) + \gamma_\varphi\left(2\sigma_{ee}\hat{Q}\sigma_{ee} - \hat{Q}\sigma_{ee} - \sigma_{ee}\hat{Q}\right),\end{aligned} \tag{S.8}$$

where $\kappa_a\,(\kappa_b)$ is the decay rate of cavity mode $a(b)$, $\gamma_{\parallel}$ is the depolarizing rate of mediated flux qubit, γ_φ is its dephasing rate, and the qubit's total relaxation rate is $\gamma_\perp = \gamma_{//}/2 + \gamma_\varphi$. $\kappa_a = \kappa_{a0} + \kappa_{c1}$ ($\kappa_b = \kappa_{b0} + \kappa_{c2}$) consists of the intrinsic damping rate κ_{a0} (κ_{b0}) and the coupling loss κ_{c1} (κ_{c2}) induced by the input transmission line.

In the strong dispersive regime, we can neglect the evolution of the off-diagonal elements of the qubit state and let $\dot{\sigma}_+ = \dot{\sigma}_- = 0$, by which we have

$$\sigma_{-}=\frac{g_a a\sigma_z+g_b b\sigma_z}{\Delta_q-i\gamma_\perp},\ \sigma_{+}=\frac{g_a a^\dagger\sigma_z+g_b b^\dagger\sigma_z}{\Delta_q+i\gamma_\perp}. \tag{S.9}$$

Taking $\hat{Q}=\sigma_z$ in Eq. (S.6), we can obtain

$$\dot{\sigma}_z=-\gamma_{//}\sigma_z-2ig_a\left(-a^\dagger\sigma_{-}+a\sigma_{+}\right)-2ig_b\left(-b^\dagger\sigma_{-}+b\sigma_{+}\right)-\gamma_{//}. \tag{S.10}$$

By substituting Eq. (S.9) into Eq. (S.10), we can obtain the approximate expression of σ_z by letting $\dot{\sigma}_z=0$ and expanding up to the second order term of $\delta^{-1}=\left[\Delta_q^2+\gamma_\perp^2\right]^{-1}$ as

$$\begin{aligned}\sigma_z\approx-1+\frac{1}{\gamma_{//}\delta}\left\{4\gamma_\perp\left(g_a^2a^\dagger a+g_b^2b^\dagger b\right)+4g_ag_b\gamma_\perp\left(a^\dagger b+ab^\dagger\right)\right\}\\-\frac{1}{\gamma_{//}\delta^2}\left\{16\gamma_\perp^2\left[g_a^4a^\dagger aa^\dagger a+g_b^4b^\dagger bb^\dagger b\right]\right\}.\end{aligned} \tag{S.11}$$

By substituting Eq. (S.9) and Eq. (S.11) into the dynamical equations of cavity modes a and b, we can obtain

$$\begin{aligned}\dot{a}=&-i\left(\Delta_a-\frac{i\kappa_a}{2}\right)a+i\left(g_a^2a+g_ag_bb\right)\frac{\left(\Delta_q+i\gamma_\perp\right)}{\delta}\\&-\frac{i\left(\Delta_q+i\gamma_\perp\right)}{\gamma_{//}\delta^2}\begin{bmatrix}4\gamma_\perp\left(g_a^4aa^\dagger a+g_a^2g_b^2ab^\dagger b+g_a^3g_ba^\dagger ab+g_ag_b^3bb^\dagger b\right)\\+4\gamma_\perp\left(g_a^3g_baa^\dagger b+g_a^3g_baab^\dagger+g_a^2g_b^2a^\dagger bb+g_a^2g_b^2abb^\dagger\right)\end{bmatrix},\end{aligned} \tag{S.12}$$

$$\begin{aligned}\dot{b}=&-i\left(\Delta_b-\frac{i\kappa_b}{2}\right)b+i\left(g_ag_ba+g_b^2b\right)\frac{\left[\Delta_q+i\gamma_\perp\right]}{\delta}-\frac{i\left[\Delta_q+i\gamma_\perp\right]}{\gamma_{//}\delta^2}\\&\times\left[4\gamma_\perp\left(g_a^3g_baa^\dagger a+g_ag_b^3ab^\dagger b+g_a^2g_b^2a^\dagger ab+g_b^4bb^\dagger b\right)+\ldots\right].\end{aligned} \tag{S.13}$$

We then simplify our model and expand up to the fourth-order Kerr-nonlinear terms of the two cavity modes induced by the mediated qubit, by which we can obtain the following effective Hamiltonian from Eq. (S.12) and Eq. (S.13) by eliminating the degrees of freedom of the mediated qubit

$$\begin{aligned}H_{eff}=&\left(\omega_a-g-\frac{i\kappa_a}{2}\right)a^\dagger a+\left(\omega_b-g-\frac{i\kappa_b}{2}\right)b^\dagger b-g\left(ab^\dagger+a^\dagger b\right)\\&+\mu_{kerr}\left(a^\dagger aa^\dagger a+b^\dagger bb^\dagger b\right).\end{aligned} \tag{S.14}$$

The effective coupling strength between the two cavity modes g and the effective self-Kerr coefficient μ_{kerr} can be written as

$$g = \frac{\Delta_q g_a g_b}{\Delta_q^2 + \gamma_\perp^2},\ \mu_{kerr} = \frac{4 g_{a(b)}^4 \Delta_q \gamma_\perp}{\gamma_{//}\left(\Delta_q^2 + \gamma_\perp^2\right)^2}. \tag{S.15}$$

As shown in Eq. (S.14), the effective coupling strength g can be tuned by modulating the effective frequency detuning $\Delta_q = \omega_q - \omega_d$ of the qubit. As the driving frequency ω_d is tuned to be close to ω_a, ω_b and $\omega_q >> \omega_a$, ω_b, the effective frequency detuning Δ_q can be approximated as $\Delta_q \doteq \omega_q - \omega_a$.

From the Hamiltonian in Eq. (S.14), we can analyze the phase transition in the vicinity of the exceptional point in our system. Since the Kerr nonlinearity is weak in our system, we can only consider the first three terms of Eq. (S.14), which can be rewritten as

$$\begin{aligned} \tilde{H}_{eff} &= \begin{pmatrix} a^\dagger & b^\dagger \end{pmatrix} \begin{pmatrix} \omega_a - g - \frac{i\kappa_a}{2} & -g \\ -g & \omega_b - g - \frac{i\kappa_b}{2} \end{pmatrix} \begin{pmatrix} a \\ b \end{pmatrix} \\ &= \begin{pmatrix} a_+^\dagger & a_-^\dagger \end{pmatrix} \begin{pmatrix} \omega_+ & 0 \\ 0 & \omega_- \end{pmatrix} \begin{pmatrix} a_+ \\ a_- \end{pmatrix}. \end{aligned} \tag{S.16}$$

By diagonalizing this Hamiltonian, we can obtain the eigenvalues $\omega_\pm$ as

$$\omega_\pm = \tilde{\omega}_\pm - \frac{i\kappa_\pm}{2} = \frac{\omega_a + \omega_b}{2} - g - \frac{i}{4}\left(\kappa_a + \kappa_b\right) \pm \sqrt{g^2 - \frac{1}{4}\left[i\left(\omega_a - \omega_b\right) + \frac{\kappa_a - \kappa_b}{2} \right]^2}, \tag{S.17}$$

and the corresponding supermodes are a_-, a_+. The real parts of $\omega_\pm$ represent the eigenfrequencies of the two supermodes and the imaginary parts denote the dissipative rates of the supermodes. We tune the frequency detuning between the two cavity modes $\delta_{ab} = \omega_a - \omega_b$ and the effective coupling strength g to obtain the topological diagram of the eigenfrequencies (Fig. S5a) and the dissipative rates (Fig. S5b). At zero detuning ($\omega_a = \omega_b = \omega_0$), Eq. (S.17) is simplified as

$$\omega_\pm = \omega_0 - g - \frac{i}{4}\left(\kappa_a + \kappa_b\right) \pm \sqrt{g^2 - \frac{\left(\kappa_a - \kappa_b\right)^2}{16}}. \tag{S.18}$$

It can be shown that there is an exceptional point (EP) at $g = \kappa \equiv \left|\kappa_a - \kappa_b\right|/4$, where the complex eigenvalues degenerate with each other. There are two different regimes as shown in Fig. S5c, d. (i) In the weak-coupling regime such that $g < \kappa$, which is also

called the passive PT-symmetry-broken regime, the imaginary parts of $\omega_{\pm}$ are splitting, while the real parts of $\omega_{\pm}$ are degenerate at $\tilde{\omega}_0 \equiv \omega_0 - g$. This frequency shift from ω_0 to $\tilde{\omega}_0$ is induced by the interaction between the qubit and the cavity modes in the large-dispersive regime known as the ac-Stark shift of the cavity mode. (ii) In the strong-coupling regime such that $g > \kappa$, which is also called the passive PT-symmetric regime, the imaginary parts of $\omega_{\pm}$ are degenerate while the real parts of $\omega_{\pm}$ are splitting. Thus, the two supermodes have different eigenfrequencies but the same dissipative rate.

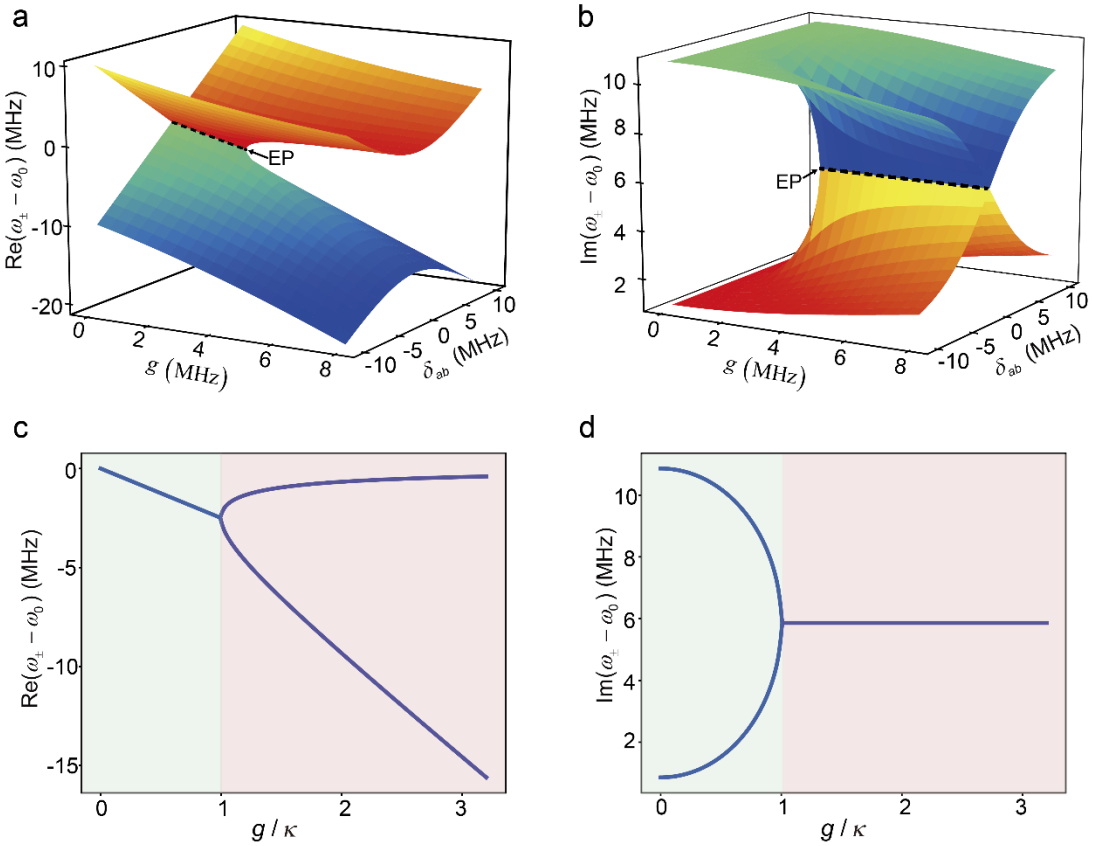

Figure S5. Topology of non-Hermitian degeneracy. Topological evolutions of the real (**a**) and imaginary (**b**) parts of the eigenvalues of the coupled resonators with changing coupling strength g and the frequency detuning between the two cavity modes $\delta_{ab} = \omega_a - \omega_b$. The real and imaginal parts of the eigenvalues when $\omega_a = \omega_b = \omega_0$ are shown in **c** and **d.**

C. Experimental setup of the bifurcation and the nonreciprocity measurement

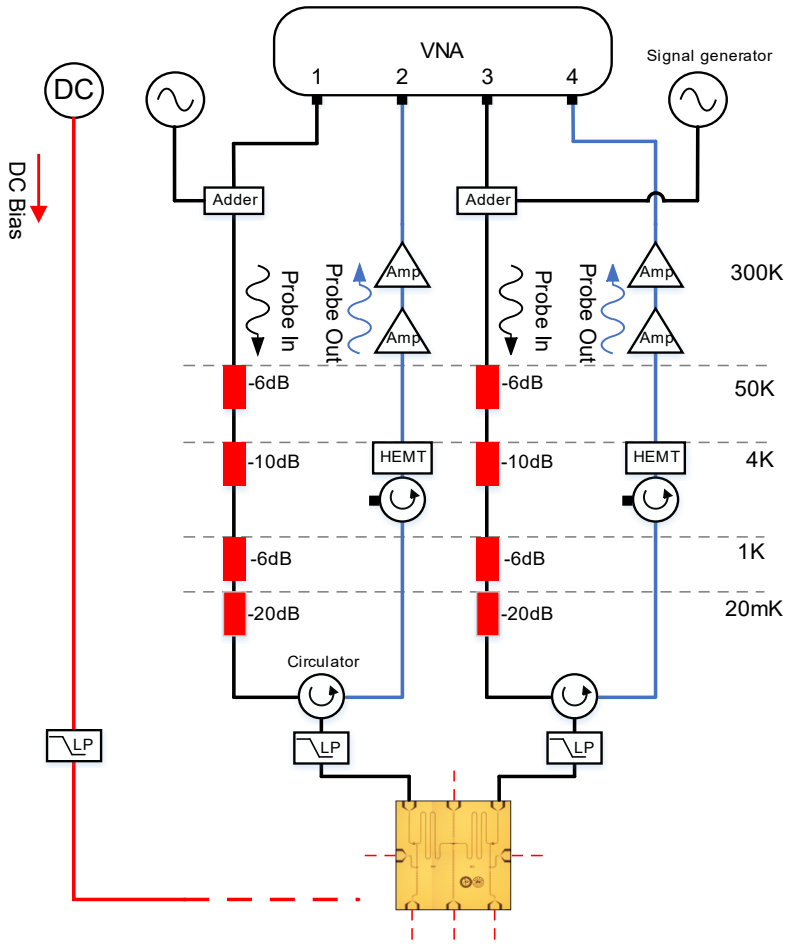

Figure S6. Schematic diagrams of the measurement circuits for the bifurcation and the nonreciprocity measurement. The two input lines are connected to port 1 and port 3 of VNA while the two output lines are connected to the port 2 and port 4 of VNA. We add two signal generators in two input lines for the two-tone measurement.

D. Experimental data for the bifurcation in the vicinity of EP

After we tune the two cavity modes to be resonant with each other and calibrate the attenuations in the two input lines, we can tune the effective coupling between the two cavity modes by the quantum coupler (Fig. S7) and find the exceptional point using the measurement circuits in Fig. S6.

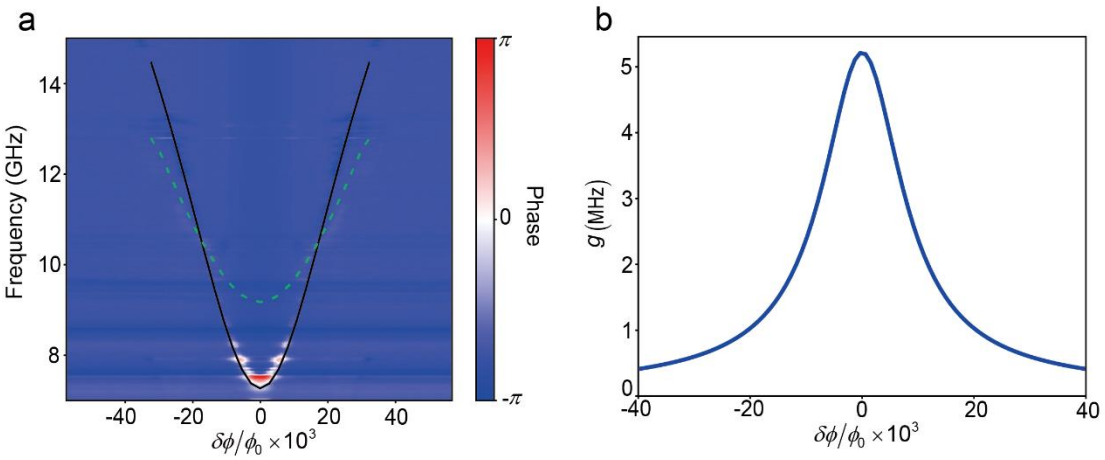

Figure S7. Illumination of the tuneable coupling strength between the two resonators with a flux qubit as a quantum coupler. a, Intensity plot of the phase of a transmission signal as a function of the driving frequency and $\delta\Phi$ for the mediated qubit. The dash lines are the theoretical fitting curves for energy levels obtained from the full Hamiltonian of flux qubit, corresponding to the single-photon transition from the ground state to the first excited state (E_{01}, solid black line) and the two-photon transition from the ground state to the second excited state ($E_{02}/2$, dashed green line), respectively. **b,** The calculated effective coupling strength g between the two resonators versus the biased magnetic flux $\delta\Phi$.

We show the reflection coefficient of cavity b (S_{43}) versus different external magnetic fields in the main loop ($\delta\Phi$) of the quantum coupler in Fig. S8. Here, the average photon numbers $\langle n_a \rangle$ of the probe field are less than 1. The energy levels of the quantum coupler are shown in Fig. S8a. A dip in the reflection spectrum can be observed when the E_{01} frequency of the quantum coupler is far away from the frequencies of the two cavity modes, while a mode-splitting in the reflection coefficient spectrum can be seen when the frequency of the quantum coupler is close to those of the cavity modes. The exceptional points can be found in the crossover regions. The asymmetric splitting in the strong-coupling regime indicates that the coupled system works in the quantum regime.

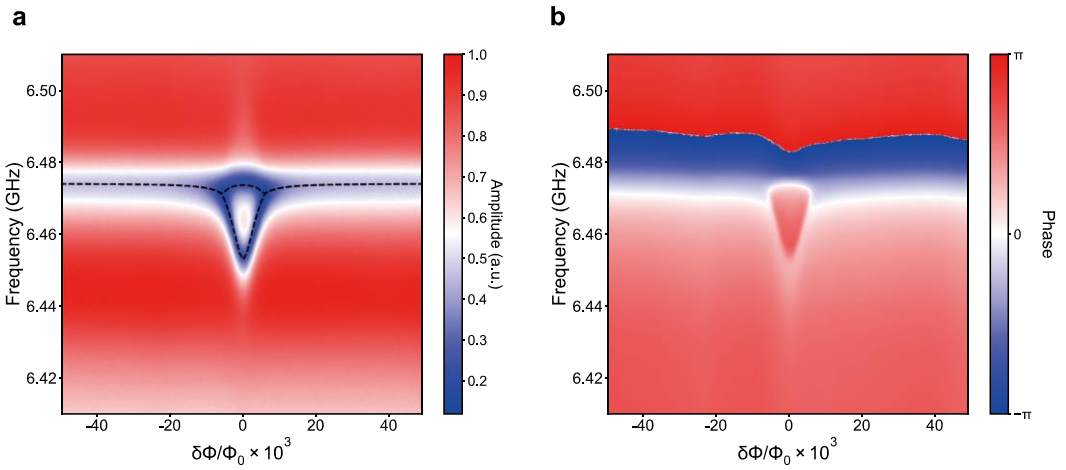

Figure S8. Bifurcation in the vicinity of the exceptional point by applying external magnetic fields to the quantum coupler. The amplitude (**a**) and phase (**b**) of the reflection coefficient spectrum of cavity b (S_{43}) versus the external magnetic field in the main loop of the quantum coupler. The dashed lines are the theoretical curves of the frequencies of the supermodes.

E. Extracting the complex frequencies of the supermodes

Because the measurement circuit background is fluctuating and there is minor nonlinearity in the two cavities, the reflection spectra are not perfect Lorentzian shapes. Therefore, we cannot extract the accurate complex frequency by just a simple Lorentzian fitting. We extract the real part of the complex frequency by finding the extreme points of the polynomial fit, and extract the imaginary part by a one-dip or two-dip Lorentzian fitting curve with fixed frequencies.

We first fit the reflection spectrum of the right cavity by using a polynomial fitting, after getting the polynomial function f(x), then calculate the first derivative function $f^{'}(x)$ and second derivative function $f^{''}(x)$. Get the local minimum points by solving the roots of $f^{'}(x_0)=0$ when $f^{''}(x_0)>0$. In the direction that the coupling strength increases, the number of the local minimum points changes from one to two, thus we know that we catch the exceptional point. We plot the frequencies of local minimum points as the real part of the complex frequency. Next step is getting the imaginary part of the complex frequency. In the strong-coupling regime, we fit the reflection spectra

of the right cavity with a two-dip Lorentzian function

$$L = a + a_0 \frac{w}{4(x - x_0) + w^2} + a_1 \frac{w}{4(x - x_1) + w^2},$$

where $w = \kappa_{a/b} / 2\pi$ is the linewidth, a is the offset, a_0 and a_1 are the scaling factors, and x_0, x_1 are the centers of the two dips with fixed center frequencies. Here, x_0 and x_1 are gotten from the two local minimum points. In the weak coupling regime, we fit the reflection spectra of the left cavity with a one-dip Lorentzian function

$$\tilde{L} = a + a_0 \frac{w}{4(x - x_0) + w^2},$$

where $w = \kappa_a / 2\pi$ is the linewidth, a is the offset, a_0 is the scaling factors, and x_0 is the center of the dip with fixed center frequency. Note that x_0 is gotten from the one local minimum point. After this one-dip Lorentzian fitting, we get one of the imaginary branch $\mathrm{Im}(\omega_+)$, and another imaginary branch $\mathrm{Im}(\omega_-)$ is calculated directly with $(\kappa_a + \kappa_b) - \mathrm{Im}(\omega_+)$. The fitting details are shown in Fig. S9.

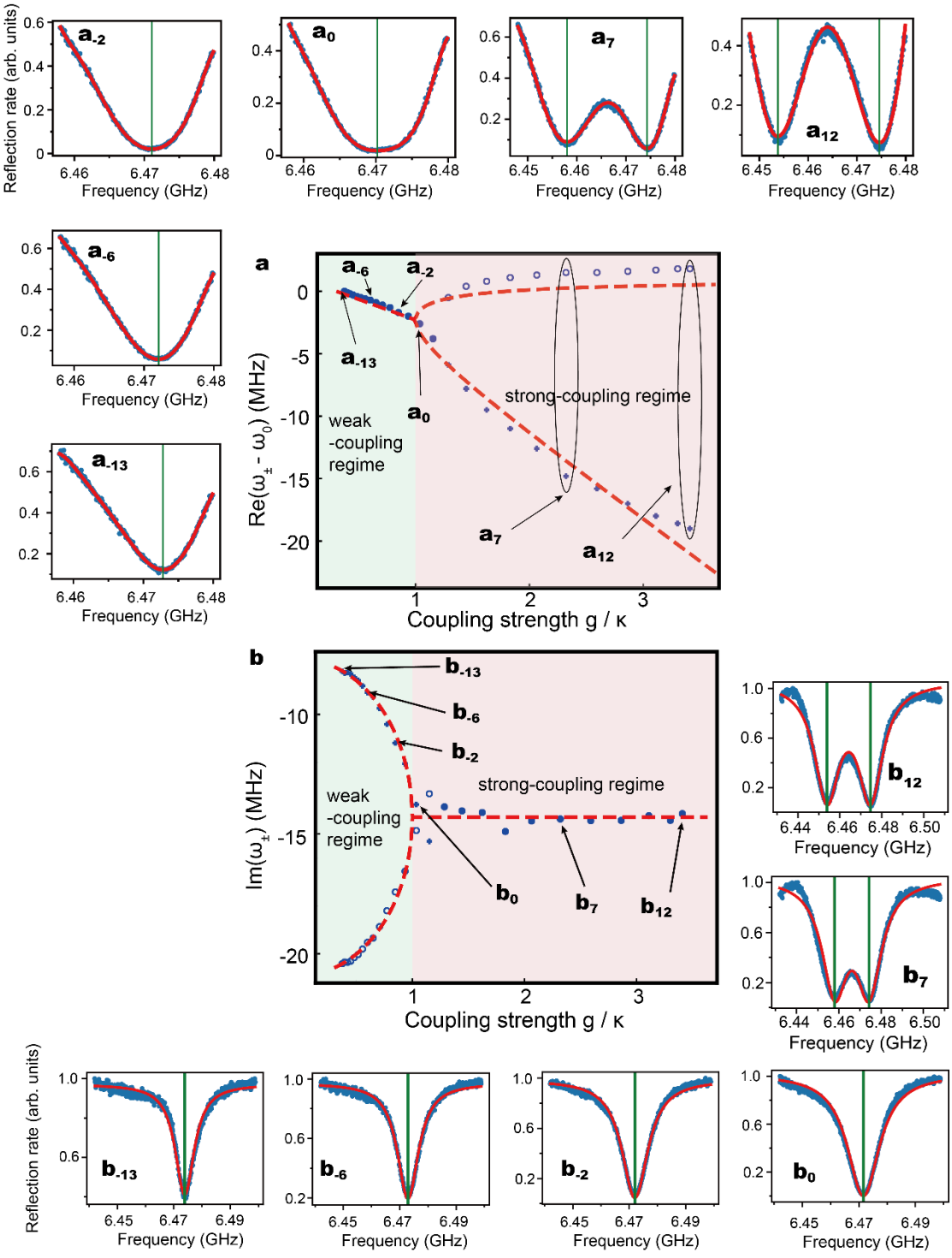

Figure S9. Curve fitting details for extracting the complex frequencies of the supermodes. a$_{-13}$ - a$_{12}$, Polynomial fittings of the right cavity spectra to extract the real parts of the supermodes. The real parts are gotten from the one or two local minimum points of every polynomial fitting. **b$_{-13}$ - b$_{12}$**, The one-dip Lorentzian fittings of the left cavity spectra (in the weak-coupling regime) and the two-dip Lorentzian fittings of the right cavity spectra (in the strong-coupling regime).

III. FEW-PHOTON NON-RECIPROCAL TRANSMISSION

A. Simulation of nonreciprocity

Through the analysis in Supplementary Part III Section B, we know that nonlinearity will be localized in the high-Q cavity in the weak-coupling regime, which will introduce nonreciprocal transport of photons. When the microwave signal is fed into the high-Q cavity a, it will be transmitted to the low-Q cavity b due to the coupling between the two cavities. The output fields from the two cavities can be represented by [S8]

$$\left\langle a_{ref} \right\rangle = \left\langle a_{in} \right\rangle + \sqrt{\kappa_a} \left\langle a \right\rangle, \tag{S.19}$$

$$\left\langle a_{trans} \right\rangle = \sqrt{\kappa_b} \left\langle b \right\rangle, \tag{S.20}$$

where $\left\langle a_{in} \right\rangle$ is the average amplitude of the input field and $\left\langle a \right\rangle$ is the expectation of the cavity mode a in steady state. In our system, the input microwave field is a coherent state at few-photon level and the Hamiltonian of the driving field can be written as $H_d = i\left[\Omega_d \left(a^\dagger - a\right)\right]/2$. Thus, the average amplitude of the input field is $\left\langle a_{in} \right\rangle = -\Omega_d \Big/ \left(2\sqrt{\kappa_a}\right)$ and the total Hamiltonian is $H = H_1 + H_d$, where H_1 is expressed in Eq. (S.6) with $\Delta_{a(b)} = \Delta_0 \equiv \omega_0 - \omega$. The master equation of the total system can be expressed as

$$\frac{d}{dt}\hat{\rho} = -i\left[H, \rho\right] + \kappa_a \mathcal{D}\left[a^\dagger\right]\rho + \kappa_b \mathcal{D}\left[b^\dagger\right]\rho + \gamma_\parallel \mathcal{D}\left[\sigma_-\right]\rho + 2\gamma_\varphi \mathcal{D}\left[\sigma_z\right]\rho, \tag{S.21}$$

where the Lindblad superoperator can be written as $\mathcal{D}[a]\rho = a\rho a^\dagger - aa^\dagger\rho/2 - \rho aa^\dagger/2$. We have omitted the thermal noise in Eq. (S.21). By letting $d\hat{\rho}/dt = 0$, we can get the stationary value of $\left\langle a \right\rangle$. Therefore, the normalized transmission T from cavity a to cavity b (forward) and the reflection R from the cavity a can be expressed as

$$T_{a\to b} = \left|\frac{\left\langle a_{trans} \right\rangle}{\left\langle a_{in} \right\rangle}\right|^2 = \left|\frac{\sqrt{\kappa_b}\left\langle b \right\rangle}{\Omega_d / 2\sqrt{\kappa_a}}\right|^2, \tag{S.22}$$

$$R_a = \left|\frac{\left\langle a_{ref} \right\rangle}{\left\langle a_{in} \right\rangle}\right|^2 = \left|1 - \frac{\sqrt{\kappa_a}\left\langle a \right\rangle}{\Omega_d / 2\sqrt{\kappa_a}}\right|^2. \tag{S.23}$$

Analogously, when the probe signal is fed into the low-Q cavity b, the Hamiltonian of

the driving field will be expressed as $H_d^{'} = \frac{i\Omega_d}{2}\left(b^{\dagger} - b\right)$ and the normalized transmission T from cavity b to cavity a (backward) can be written as

$$T_{b\to a} = \left|\frac{\langle b_{trans}\rangle}{\langle b_{in}\rangle}\right|^2 = \left|\frac{\sqrt{\kappa_a}\langle a\rangle}{\Omega_d / 2\sqrt{\kappa_b}}\right|^2. \tag{S.24}$$

We can define the isolation ratio as

$$I = 10\log(T_{b\to a} / T_{a\to b}). \tag{S.25}$$

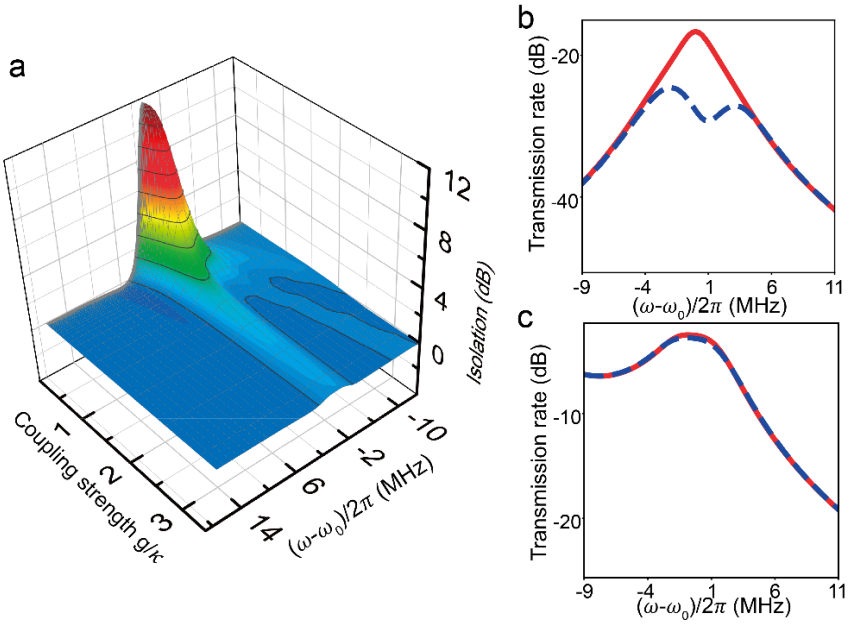

Figure S10. Numerical simulations of the unidirectional transmission. a, Isolation ratio versus different probe frequencies $(\omega - \omega_0)$ and different effective coupling strengths g/κ. **b,** Comparison of forward (dashed blue line) and backward (solid orange line) transmissions in the weak-coupling regime. **c,** The forward (dashed blue line) and backward (solid orange line) transmissions in the strong-coupling regime.

From Eqs. (S.21), (S.22), (S.24) and (S.25), we use *Qutip* to give numerical simulations [S9] of the isolation ratio by changing ω and g_{eff} in Fig. S10a. We can see that the isolation ratio in weak-coupling regime can be large enough to reach 12 dB which agrees well with experimental value 10.1 dB, while in strong-coupling regime the isolation ratio is zero. From the transmission spectra in Fig. S10b and c, it can be seen that the transmission signal will be suppressed when traveling backward in weak-coupling regime. Additionally, as shown in Fig. S10c, the nonreciprocal phenomena exist only when the probe frequency is close to the real part of eigenvalues in Eq. (S.18),

i.e., the eigenfrequencies of the supermodes. In fact, when the probe field is off-resonant with the supermodes, the photon cannot enter the cavity and thus the nonreciprocal phenomenon will be suppressed.

As shown in Fig. S11a, the isolation ratio turns to be zero when the average photon number of the input field is less than 0.5, which means that the nonreciprocal effects will be suppressed with the decrease of the strength of the input field. In fact, the nonreciprocal transmission of photon appeared in the weak-coupling regime is induced by the localization of the intracavity photons in the high-Q cavity. These localization effects will be suppressed with the decrease of strength of the input field due to the increasing effects induced by the quantum noises. The nonreciprocal transmission of photon is also induced by the enhanced nonlinearity in the vicinity of the exceptional point. This enhanced nonlinearity will also be weakened with the decrease of the strength of the input field. As shown in Fig. S11b, the forward transmission power increases almost linearly with the average driven photon numbers in the strong-coupling regime, but nonlinearly in the weak-coupling regime. With the decrease of the strength of the input field, the increasing noise effects and the weakened nonlinearity will greatly suppress the forward transmission, and thus lead to the decrease of the isolation ratio.

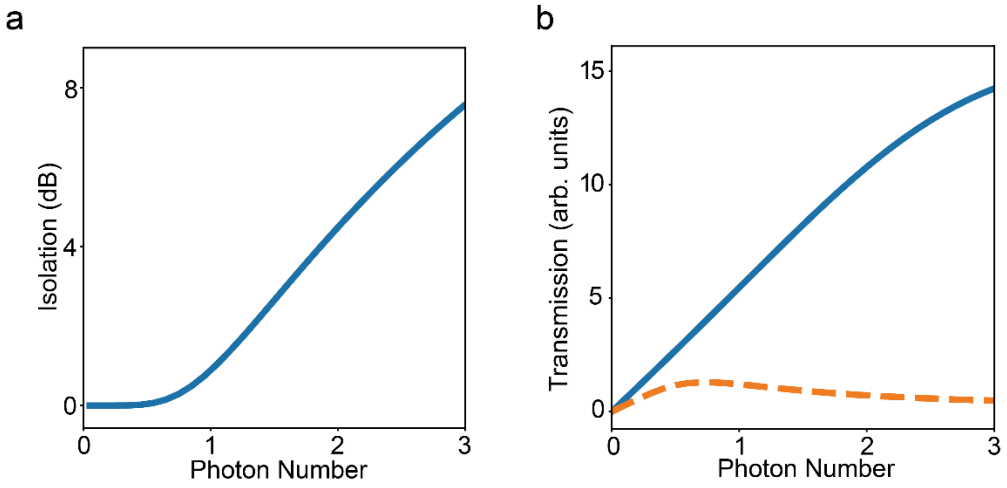

Figure S11. Numerical simulations of the suppressed non-reciprocal transmission with deceasing input photon numbers. a, The isolation ratios versus the input photon numbers. **b,** The forward output powers versus the input photon number in the strong-coupling regime (solid blue line) and the weak-coupling regime (dashed orange line).

B. Amplified nonlinearity in the vicinity of the exceptional point

In this part, we will show the mechanism of the amplified nonlinearity in the vicinity of the exceptional point. There is a transformation matrix P between supermodes and the cavity modes, which can be expressed as

$$\begin{pmatrix} a_+ \\ a_- \end{pmatrix} = P \begin{pmatrix} a \\ b \end{pmatrix}, \tag{S.26}$$

where

$$P = \frac{\begin{pmatrix} -g & \left[\left(\tilde{\omega}_- - \tilde{\omega}_0 \right) - \frac{i}{2} \left(\kappa_- - \kappa_b \right) \right] \\ -g & \left[\left(\tilde{\omega}_+ - \tilde{\omega}_0 \right) - \frac{i}{2} \left(\kappa_+ - \kappa_b \right) \right] \end{pmatrix}}{\sqrt{g^2 + \left(\tilde{\omega}_\mp - \tilde{\omega}_0 \right)^2 + \left(\kappa_\mp - \kappa_b \right)^2 / 4}}. \tag{S.27}$$

From Eq. (S.17) and Eq. (S.27), we have

$$\begin{aligned} a &= -\frac{\sqrt{g^2 + \left(\tilde{\omega}_- - \tilde{\omega}_0 \right)^2 + \frac{\left(\kappa_- - \kappa_b \right)^2}{4}} P_{22}}{g \left[\left(\tilde{\omega}_+ - \tilde{\omega}_- \right) - \frac{i}{2} \left(\kappa_+ - \kappa_- \right) \right]} a_+ + \frac{\sqrt{g^2 + \left(\tilde{\omega}_+ - \tilde{\omega}_0 \right)^2 + \frac{\left(\kappa_+ - \kappa_b \right)^2}{4}} P_{12}}{g \left[\left(\tilde{\omega}_+ - \tilde{\omega}_- \right) - \frac{i}{2} \left(\kappa_+ - \kappa_- \right) \right]} a_- \\ &\triangleq \alpha_+ a_+ + \alpha_- a_-, \end{aligned} \tag{S.28}$$

$$\begin{aligned} b &= -\frac{\sqrt{g^2 + \left(\tilde{\omega}_- - \tilde{\omega}_0 \right)^2 + \frac{\left(\kappa_- - \kappa_b \right)^2}{4}}}{\left[\left(\tilde{\omega}_+ - \tilde{\omega}_- \right) - \frac{i}{2} \left(\kappa_+ - \kappa_- \right) \right]} a_+ + \frac{\sqrt{g^2 + \left(\tilde{\omega}_+ - \tilde{\omega}_0 \right)^2 + \frac{\left(\kappa_+ - \kappa_b \right)^2}{4}}}{\left[\left(\tilde{\omega}_+ - \tilde{\omega}_- \right) - \frac{i}{2} \left(\kappa_+ - \kappa_- \right) \right]} a_- \\ &\triangleq \beta_+ a_+ + \beta_- a_-. \end{aligned} \tag{S.29}$$

The Kerr term in Eq. (S.14) can be written as

$$H_{kerr} = \mu_{kerr} \left[\left(\left| \alpha_- \right|^2 a_-^\dagger a_- + \left| \alpha_+ \right|^2 a_+^\dagger a_+ \right)^2 + \left(\left| \beta_- \right|^2 a_-^\dagger a_- + \left| \beta_+ \right|^2 a_+^\dagger a_+ \right)^2 \right]. \tag{S.30}$$

We then consider the cross Kerr term in the supermode picture

$$H_{kerr}^{'} = \mu' a_+^\dagger a_+ a_-^\dagger a_-, \tag{S.31}$$

where $\mu' = 2\mu_{kerr} \left(\left| \alpha_+ \right|^2 \left| \alpha_- \right|^2 + \left| \beta_+ \right|^2 \left| \beta_- \right|^2 \right)$. It can be shown that μ' can be represented in the strong-coupling regime and the weak-coupling regime as

$$\mu_s^{'}=\frac{g^4\mu_{kerr}}{\left(g^2-\frac{\left(\kappa_a-\kappa_b\right)^2}{16}\right)^2},\ \mu_b^{'}=\frac{\left(\kappa_a-\kappa_b\right)^2 g^2\mu_{kerr}}{16\left(\frac{\left(\kappa_a-\kappa_b\right)^2}{16}-g^2\right)^2}. \tag{S.32}$$

In the weak-coupling regime, the field is localized in the high-Q resonator. Thus, we can omit the field in the low-Q cavity and the supermodes can be approximated as

$$a_+\approx\frac{-g}{\sqrt{g^2+\left(\tilde{\omega}_--\tilde{\omega}_0\right)^2+\left(\kappa_--\kappa_b\right)^2/4}}a,$$

$$a_-\approx\frac{-g}{\sqrt{g^2+\left(\tilde{\omega}_+-\tilde{\omega}_0\right)^2+\left(\kappa_+-\kappa_b\right)^2/4}}a. \tag{S.33}$$

Therefore, the cross Kerr term can be written as Eq. (S.34), which means that the cross Kerr will introduce self-Kerr effect in the high-Q cavity,

$$H_{kerr}^{'}\approx\frac{g^4\mu}{4\left(\frac{\left(\kappa_a-\kappa_b\right)^2}{16}-g^2\right)^2}\left(a^{\dagger}a\right)^2. \tag{S.34}$$

Reference:

[S1] Orlando, T. P., Mooij, J. E., Tian, L. van der Wal, C. H., Levitov, L. S., Lloyd, S. & Mazo, J. J. Superconducting persistent-current qubit. *Phys. Rev. B* **60**, 15398-15413 (1999).

[S2] Peng, Z. H., Liu, Yu-xi, Peltonen, J. T., Yamamoto, T., Tsai, J. S. & Astafiev, O. Correlated emission lasing in harmonic oscillators coupled via a single three-level artificial atom, *Phys. Rev. Lett.* **115**, 223603 (2015).

[S3] Baust, A., Hoffmann, E., Haeberlein, M., Schwarz, M. J., Eder, P., Goetz, J., Wulschner, F., Xie, E., Zhong, L., Quijandría, F., Peropadre, B., Zueco, D., García Ripoll, J.-J., Solano, E., Fedorov, K., Menzel, E. P., Deppe, F., Marx, A. & Gross, R. Tunable and switchable coupling between two superconducting resonators, *Phys. Rev. B* **91**, 014515 (2015).

[S4] Blais, A., Huang, R.-S., Wallraff, A., Girvin, S. M. & Schoelkopf, R. J. Cavity quantum electrodynamics for superconducting electrical circuits: An architecture for quantum computation. *Phys. Rev. A* **69**, 062320 (2004).

[S5] Schuster, D. I., Wallraff, A., Blais, A., Frunzio, L., Huang, R. S., Majer, J., Girvin,

S. M. & Schoelkopf, R. J. ac Stark shift and dephasing of a superconducting qubit strongly coupled to a cavity field. *Phys. Rev. Lett.* **94**, 123602 (2005).

[S6] Xia, K., & Twamley, J. All-optical switching and router via the direct quantum control of coupling between cavity modes. *Phys. Rev. X* **3**, 1–11 (2013).

[S7] Minganti, F., Miranowicz, A., Chhajlany, R. W., & Nori, F. Quantum exceptional points of non-Hermitian Hamiltonians and Liouvillians: The effects of quantum jumps. *Phys. Rev. A* **100**, 1–19 (2019).

[S8] Gardiner, C. W., & Collett, M. J. Input and output in damped quantum systems: Quantum stochastic differential equations and the master equation. *Phys. Rev. A* **31**, 3761–3774 (1985).

[S9] Johansson, J. R., Nation P. D. & Nori F. QuTiP: An open-source Python framework for the dynamics of open quantum systems. *Comp. Phys. Comm.* **183**, 1760 (2012).